

## Exchange Processes Induced by Large Horizontal Coherent Structures in Floodplain Vegetated Channels

Truong, S. H.; Uijttewaal, W. S.J.; Stive, M. J.F.

**DOI**

[10.1029/2018WR022954](https://doi.org/10.1029/2018WR022954)

**Publication date**

2019

**Document Version**

Final published version

**Published in**

Water Resources Research

**Citation (APA)**

Truong, S. H., Uijttewaal, W. S. J., & Stive, M. J. F. (2019). Exchange Processes Induced by Large Horizontal Coherent Structures in Floodplain Vegetated Channels. *Water Resources Research*, 55(3), 2014-2032. <https://doi.org/10.1029/2018WR022954>

**Important note**

To cite this publication, please use the final published version (if applicable). Please check the document version above.

**Copyright**

Other than for strictly personal use, it is not permitted to download, forward or distribute the text or part of it, without the consent of the author(s) and/or copyright holder(s), unless the work is under an open content license such as Creative Commons.

**Takedown policy**

Please contact us and provide details if you believe this document breaches copyrights. We will remove access to the work immediately and investigate your claim.



## RESEARCH ARTICLE

10.1029/2018WR022954

## Exchange Processes Induced by Large Horizontal Coherent Structures in Floodplain Vegetated Channels

## Key Points:

- Vegetation has large influences on flow in floodplains, even outside the vegetated area through large horizontal coherent structures (LHCSSs)
- Large horizontal coherent structures can have an influence over a larger transverse distance than their penetration into the vegetation
- Reducing the mangrove width results in more frequent LHCSSs, increasing the momentum exchange and erosive forces at the vegetation interface

## Correspondence to:

S. H. Truong and W. S. J. Uijttewaal, s.truonghong@tudelft.nl; W.S.J.Uijttewaal@tudelft.nl

## Citation:

Truong, S. H., Uijttewaal, W. S. J., & Stive, M. J. F. (2019). Exchange processes induced by large horizontal coherent structures in floodplain vegetated channels. *Water Resources Research*, 55. <https://doi.org/10.1029/2018WR022954>

Received 20 MAR 2018

Accepted 5 FEB 2019

Accepted article online 12 FEB 2019

Truong S. H.<sup>1,2</sup> , W. S. J. Uijttewaal<sup>1</sup> , and M. J. F. Stive<sup>1</sup>

<sup>1</sup>Hydraulic Department, Faculty of Civil Engineering and Geosciences, Delft University of Technology, The Netherlands, <sup>2</sup>Hydraulic Department, Faculty of Civil Engineering, Thuy Loi University, Vietnam

**Abstract** Mangrove forests along the Mekong delta estuaries are usually observed to degrade together with the increasing extension of fish farms. In this limited-width condition, the formation of coherent structures, their interactions with mangroves, the role of the width of the mangrove forest, and their effects on the exchange processes between the open channel and the adjacent floodplain are still not well examined. In order to obtain more insight, a unique laboratory experiment of a vegetated compound channel mimicking estuarine mangroves has been conducted. The results show that in a compound vegetated channel with a very gentle transverse slope, the vegetated shear layer dynamics resembled that associated with vegetation rather than that associated with a depth differential. Furthermore, the flow field under the effect of large horizontal coherent structures (LHCSSs) shows a spatially and temporally cycloid motion with associated flow events, namely, sweep, ejection, stagnant, and reverse flows. It is also suggested that the coherent structures can have an influence on a broader area than the vegetation area into which the eddy structures can penetrate. In terms of the exchange processes, the momentum transfer and the intensity of transverse fluctuations induced by the LHCSSs can be related to this phenomenon. Consequently, decreasing the mangrove width can significantly affect the pattern of the LHCSSs, disturb the transverse exchange processes induced by these structures, and thereby changing the shear layer, creating unfavorable conditions for sedimentation inside forests and for river bank stability.

## 1. Introduction

Along the Mekong estuaries, mangroves have rapidly been destroyed, largely due to conversion into fish-ponds. The mangrove areas remaining have been squeezed into narrow strips often as small as 50 m (Figure 1). Riverbanks at those locations are usually suffering from erosion with an average rate of 3 m/year.

Phan et al. (2015) and Truong et al. (2017) recently strengthened the hypothesized correlation between coastal and estuarine mangrove squeeze and shore or bank erosion, respectively, for the Mekong Delta with the explicit condition that they considered regions where sediment availability is not a restriction. The estuarine mangrove squeeze is the phenomenon in which the width of the mangroves is restricted causing the degradation of mangrove forests as well as the erosion of the river banks (Truong et al., 2017). It is hypothesized that a critical minimum width of the mangrove areas is required for the survival of the ecosystem, whether the impacts come from natural causes, such as increasing relative sea-level rise or from human activities, such as spatial squeeze, these causes are highly similar in terms of impact. In a physical sense, active energetic processes require physical space to be able to absorb erosive forces and subsequently restore the impact. The mangroves need these conditions as well to be able to follow a bio-cyclic evolution.

In the estuarine mangrove squeeze areas, the forest width is usually observed to be between about 50 and 600 m, which is small compared to the width of the main channel (about 1,000 to 2,000 m). Under these conditions, the presence of lateral tidal creeks in those areas is hardly observed and can be ignored. The main interaction is the lateral exchange through the mixing layer between the main river channel and the vegetated floodplain region. In this sense, the hydrodynamics of a mangrove forest is similar to that of a vegetated floodplain channel (Mazda et al., 1997; Truong et al., 2017; see Figure 1).

Many researchers have studied the flow field and exchange mechanisms in straight and meandering, vegetated and nonvegetated channels, with or without the consideration of a floodplain. In recent decades,

©2019. The Authors.

This is an open access article under the terms of the Creative Commons Attribution-NonCommercial-NoDerivs License, which permits use and distribution in any medium, provided the original work is properly cited, the use is non-commercial and no modifications or adaptations are made.

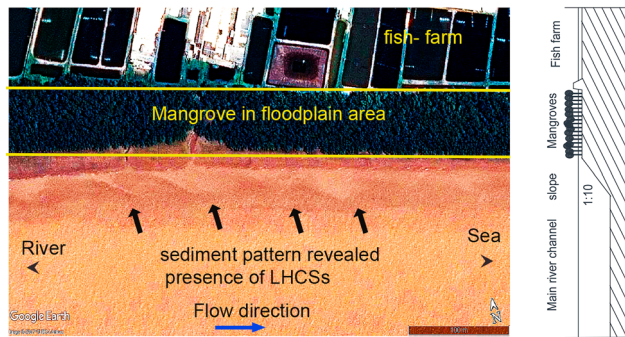


**Figure 1.** Typical mangroves distribution along a straight part of Tieu estuary, Vietnam, and the associated schematized bathymetry. Fish farms constructed close to the water boundary push the mangrove into a narrow fringe zone. This area is suffering from erosion with a rate of about 2.5 m/year (Truong et al., 2017). LHCS = large horizontal coherent structure.

the large horizontal coherent flow structures (LHCSSs) which are very large compared to the length scale of water depth and caused by the Kelvin-Helmholtz instability formed at the interface of the low flow and fast flow region have been identified to play a significant role in the lateral momentum exchange (Nadaoka & Yagi, 1998; Nezu & Onitsuka, 2001; Tamai et al., 1986; van Prooijen et al., 2005; White & Nepf, 2007, 2008; Xiaohui & Li, 2002; Zong & Nepf, 2010).

In a nonvegetated compound channel, the presence of the LHCSSs is mainly associated with the water depth differences between the floodplain and the open channel region. Based on experiments with a transversely steep change in depth and by varying the ratio of the floodplain depth to the main channel depth ( $D_r$ ) as well as the channel geometry, Knight et al. (2007) suggested that LHCSSs on unvegetated floodplains along compound channels are induced by a shear instability and mostly appear where  $D_r$  is less than 0.344. As the depth ratio increases ( $D_r > 0.344$ ), the large coherent structures appear less pronounced, and intermittent boils become stronger (Nezu et al., 1999).

However, in a vegetated compound channel, vegetation not only adds to friction, turbulence, and drag forces but also restricts the flow space. As a result, interactions between flow and vegetation in different areas, that is, within the canopy or at the interface are more complex. On the one hand, drag forces induced by vegetation make the velocity difference between slow and fast flowing regions significantly larger. This makes it possible for the LHCSSs to become more pronounced and stronger. Hence, even in the case of  $D_r > 0.344$ , large coherent structures in the presence of floodplain vegetation can still be observed (Knight et al., 2007). On the other hand, the presence of vegetation contributes to the blocking of the LHCSSs inside the forest, inhibiting their evolution. By dividing the mixing layer into two different zones, each of which has its own length scale, a new approach has been proposed by White and Nepf (2008). Their model makes it possible to estimate the penetration level of the LHCSSs into the vegetated region and should be considered the most up-to-date model for a vegetated channel. However, this model is based on only one set of flume experiments with rigid circular cylinders (Nepf, 2012), and the presence of shallow floodplains was not considered.

It is known that sediments tend to accumulate more inside the vegetated regions than outside of vegetation (Vargas-Luna et al., 2015). This means that the vegetated regions are usually more elevated than the adjacent areas. Furthermore, in previous studies (Table A3 in appendix), when taking into account the presence of a floodplain, the transition slope of the floodplain is usually as large as 1:1 (FCF experiment data—Knight & Shiono, 1990, 1996; Shiono & Knight, 1988, 1989, 1990) or 1:0.9 (Ikeda et al., 2000). However, in the Mekong Delta Estuary, the situation is slightly different. The transition areas between the floodplain and the open main river have a very gentle slope of around 1:10 (Truong et al., 2017). As the transition space from the main channel to the floodplain increases, the flow field has more space to adjust the fast flow in the open channel to the slow flow inside the vegetation. The mixing layer and its penetration into the floodplain are likely to be affected. In this context, a vegetated floodplain channel with a gentle transverse slope appears to represent a more natural profile for a vegetated channel than a vegetated channel with constant depth or a vegetated floodplain channel with a steep or vertical slope (Figure 1).

Moreover, it is important to note that all studies mentioned above only focused on wide vegetation regions, where the forest width is not a limiting factor and is always much larger than the lateral penetration of the mixing layer. However, in reality, for example, along the Mekong Delta estuaries, shrimp farms have increasingly been constructed, pushing mangrove forests into narrow strips. In this context, it is unknown how the flow field, as well as the LHCSSs, respond to changes of the forest width and how this so-called squeeze effect (Truong et al., 2017) affects the exchange processes. Furthermore, the exchange processes were studied only in the context of the sweep and ejection events, created as the LHCSSs move along the interface (White & Nepf, 2007). The transition period between these two successive events, that is, when a sweep is followed by an ejection has received little attentions and thereby, the role of this transformation period on the exchange processes in a vegetated compound channel is largely unknown.

In summary, although a number of studies have focused on the hydrodynamics of a floodplain vegetated channel, the flow field and related exchange processes are still unclear. This is especially true in the natural

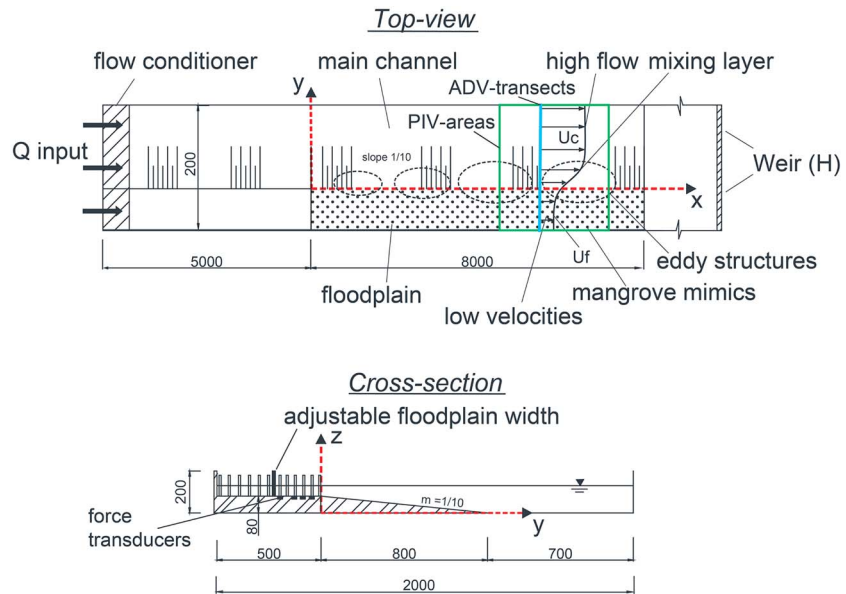


**Figure 2.** Schematic view of the experiment setup (units in mm), the presence of large coherent structures in the flow field. Not to scale. ADV = Acoustic Doppler Velocity; PIV = Particle Image Velocimetry.

cases of a gentle floodplain slope and squeeze conditions, that is, the conditions in which the width of the vegetation is restricted (Truong et al., 2017). Therefore, the main goals of this paper are to (1) evaluate the role and the effects of emergent vegetation on the hydrodynamics of a vegetated floodplain channel with a gentle transition slope, (2) to understand the effects of the LHCSs on the flow field and their related exchange processes; and (3) to relate these investigations to the squeeze effect.

## 2. Methodology

Physical modeling was chosen as a major approach. The experimental setup and measurements are described in this section. After that, the effects of vegetation are studied by comparing results in similar scenarios, with and without vegetation. Then, the significant role of the LHCSs is described, in relation to the peculiarities of the complex flow field. Finally, the squeeze effect in relation to the width of the forest is shown to play a role as it can directly affect the flows induced by the LHCSs.

The experiment was conducted in a shallow, free surface flow flume of the Fluid Mechanics Laboratory at the Delft University of Technology. The flume is 20 m long, 3 m wide, and the maximum water depth is 0.2 m. For the experiments, the width of the flume was reduced to 2 m. The average water depth-width ratio is about 1:20 and the depth-length ratio is about 1:130, creating a shallow flow condition (Jirka & Uijtewaal, 2004).

Figure 2 gives a top view and a cross-section of the experimental setup and sketches some flow features observed during the experiment. The cross-sectional profile includes a gentle floodplain slope 1:10 that mimics a typical riverbank slope as found at the Tieu estuary in the Mekong Delta. We will represent the squeeze phenomenon by varying the floodplain width to a small value such that the ratio of floodplain width and channel width  $B_f/B < 1/10$ .

Water depth and total discharge could be changed by means of a valve with a constant head tank and a downstream sharp-crested weir. Upstream from the inflow section, behind the flow straightener, a thin foam board was placed floating on the water surface to suppress small free surface oscillations. Some representative values of the flow quantities are water depth in test section  $H = 11.9$  cm; discharge  $Q = 45$  L/s; the uniform velocity in the main channel  $U_c = 32.2$  cm/s; the uniform velocity in the floodplain  $U_f = 20.9$  cm/s (no vegetation), and bottom friction coefficient  $c_f = 0.0027$ . The bottom friction parameters were determined separately for the main channel ( $c_{f,c}$ ) and for the floodplain ( $c_{f,f}$ ) according to the formula used by Uijtewaal and Booij (2000) and Chu and Babarutsi (1988):  $\frac{1}{\sqrt{c_f}} = \frac{1}{k} (\ln(\text{Re}\sqrt{c_f}) + 1.0)$ . In which  $k$  is von Karman constant (0.4) and  $Re$  is the local Reynolds number. The bottom friction coefficient was then

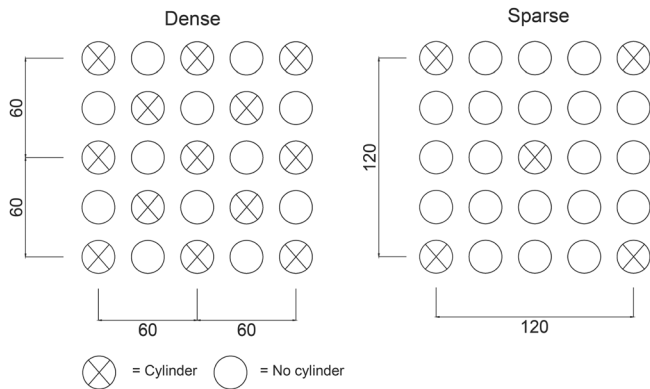


**Figure 3.** Staggered distribution of the cylinder arrays (units in mm) representative for the dense and sparse scenarios.

determined according to  $c_f = \frac{c_{f,f} + c_{f,e}}{2}$  to represent for the current scenario. With this flume configuration, a large Reynolds number (62,000) can be reached at moderate Froude numbers (0.58). In cases with vegetation, the representative values are water depth  $H = 12.2$  cm; discharge  $Q = 45$  L/s;  $U_c = 35.6$  cm/s;  $U_f = 2.1$  cm/s.

In order to obtain a proper similarity between the experimental setup and the practical situation of estuarine mangroves, the Reynolds number is also considered. In practical situations, a representative mean velocity measured inside the mangrove swamp is the order of magnitude of 0.02 m/s (Horstman, 2014) and the representative water depth is the order of magnitude of 0.1 to 0.5 m (Truong et al., 2017). This means that the Reynolds number in the floodplain is the order of magnitude of 1,000 to 10,000. In the experiment, the Reynolds number in the cylinder arrays was kept as large as possible, in the range of 1,000 to 7,500, which can be considered to be similar to the real situation. The Froude number is also kept as small as possible (in the range from 0.3 to 0.6) in order to make sure that the free surface effects are small.

Two main densities were considered in the experiment comprising sparse scenarios and dense scenarios. The densest scenarios in the experiment are similar to the sparse cases of mangroves in reality. The presence of “mangroves” in the experiment was mimicked based on the “solid volume fraction” of the mangrove which is the relation between the total volume of the plants ( $V_p$ ) and the control volume ( $V$ ):  $\Phi = V_p/V = 1 - n$ . For emergent cylinders, the solid volume fraction per unit volume can be then estimated:  $\Phi = N \cdot \pi \cdot d^2/4$ , where  $n$  is the porosity of the plants,  $d$  is the diameter of a stem, and  $N$  is the density of mangroves.

In reality, the solid volume fraction of *S.Alba* in the sparse case can be estimated to be 0.04, including both stems ( $d = 0.3$  m,  $N = 0.5$  m<sup>-2</sup>) and roots ( $d = 0.02$  m,  $N = 25$  m<sup>-2</sup>; Ranasinghe et al., 2010; Truong et al., 2017). The density of the cylinder arrays then was determined based on the solid volume fraction of *S.Alba*. Following the configuration in Figure 3, the number of cylinders ( $d = 0.01$  m) per square meter is 556 and 139, yielding a solid volume fraction value of 0.04 and 0.01, respectively. The cylinder diameter was kept relatively large in order to keep the Reynolds number based on this diameter large.

Because of the water depth difference between the floodplain and the main channel, the flow over the shallower floodplain is slower than in the deeper main channel. As a consequence of this velocity difference, a mixing layer develops between the floodplain and the channel. The transverse depth difference sustains the velocity difference and the bed friction limits the growth of the mixing layer. As the mixing layer develops, it achieves a constant width after 7 to 8 m in comparable laboratory cases with depths <0.1 m such as that of a confluence with different inflow velocities (Uijtewaal & Booij, 2000), 7.5 m in cases of a compound channel profile (Fernandes et al., 2014), and about 4 m in cases of a partly vegetated channel profile (White & Nepf, 2007). In the present experiments, velocity measurements were taken at the location where the mixing layer is expected to be fully developed, at 5 m from the first row of cylinders. This was checked and confirmed despite the slight nonuniformity due to the horizontal bed and the sloping free surface (see Figure A1 in the appendix). The middepth mean streamwise velocity was measured using an Acoustic Doppler Velocity meter (NORTEK, Vectrino) at a sampling rate of 25 Hz and the Particle Image Velocimetry (PIV) at a sampling rate of 10 Hz was applied to measure the instantaneous movement of flow at the free surface (see

**Table 1**  
Experiment Scenarios

|                         | Density 1<br>(no vegetation) | Density 2<br>(sparse vegetation) | Density 3<br>(dense vegetation) | Uncertainty |
|-------------------------|------------------------------|----------------------------------|---------------------------------|-------------|
| $\phi$                  | 0                            | 0.01                             | 0.04                            | -           |
| Cylinder/m <sup>2</sup> | 0                            | 139                              | 556                             | -           |
| $Q_{input}$ [L/s]       | 46, 60, 80                   | 46, 60, 80                       | 46, 60, 80                      | 5%          |
| $H_{control}$ [cm]      | 12, 13, 14                   | 12, 13, 14                       | 12, 13, 14                      | 2%          |
| Floodplain Width [m]    | 0.5, 0.25, 0.1               | 0.5, 0.25, 0.1                   | 0.5, 0.25, 0.1                  | 2%          |

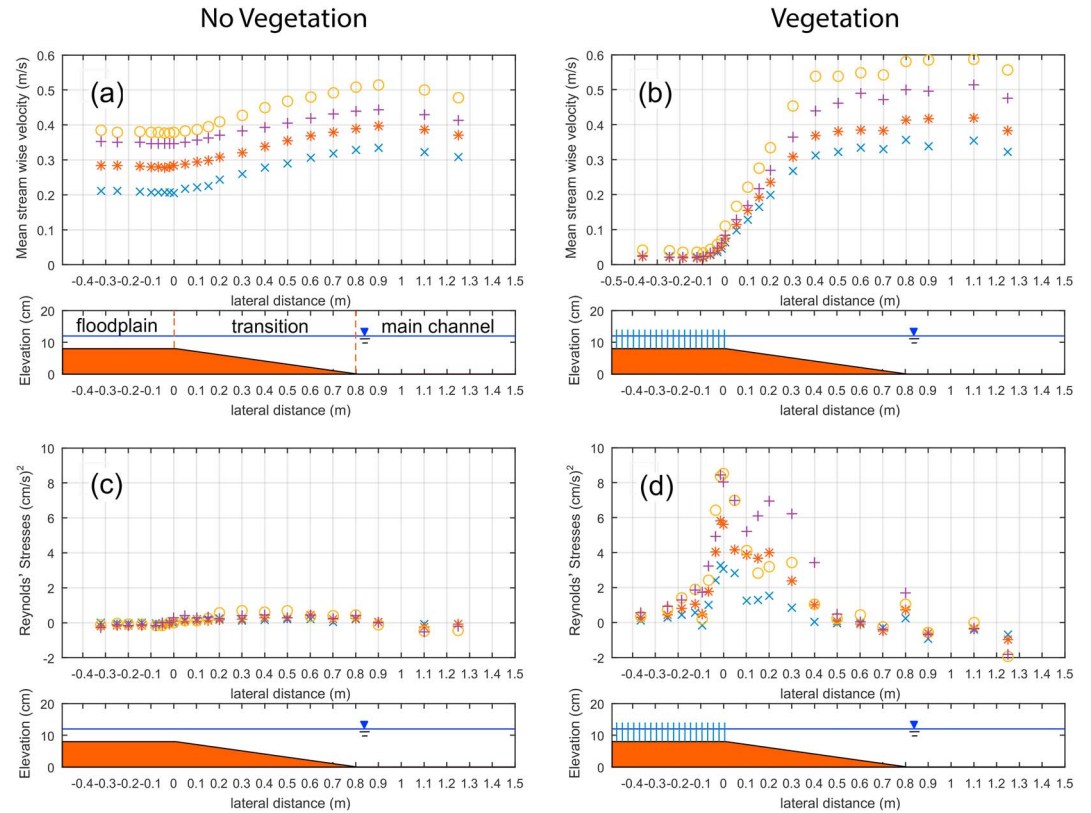


**Figure 4.** Mean streamwise velocity profile (a, b) and Reynolds shear stress  $(-\overline{u'v'})$  (c, d) in scenarios for a 50-cm-wide floodplain with no cylinders (a, c) and densely placed cylinders (b, d) configuration for different discharges and water levels. Legend qxxhyy refers to a discharge of xx L/s and a water depth of yy cm. Crosses = q45h12; stars = q60h13; pluses = q80h14; circles = q80h12.

appendix A1). Furthermore, direct measurement of the force on a single cylinder in streamwise direction was conducted to examine the drag coefficient  $C_d$ . Four sensitive force sensors were mounted under the cylinders located at different locations inside the vegetation region ( $y = -0.18, -0.06, -0.12, \text{ and } 0 \text{ m}$ ).

Following the setup described above, experiments were performed for scenarios with different discharges, water depths, and floodplain widths (Table 1). The detailed settings and description of the measurement can be found in the Appendix A1. The role of vegetation, LHCSs, floodplain width, and their corresponding effects on the flow fields in a compound channel with a gentle slope are the major interests and are analyzed in terms of the mean streamwise velocities, the Reynolds' shear stresses (RSs), the power density spectra, and the auto correlation functions ( $R_{vv}$ ) for configurations of different mangrove densities and widths. These values were determined from the data measurement according to their definitions (Pope, 2000; Uijtewaal & Booij, 2000).

### 3. Results

This section of the paper presents the experimental results. The effects of vegetation in a compound channel with a gentle slope on the shear layer dynamics at the vegetation edge were evaluated by comparing scenarios with and without vegetation. The presence of LHCSs and their influences on the flow field were clarified in terms of their flow events. Furthermore, the transverse exchange of momentum was examined and area affected by the LHCSs are deduced. Finally, the squeeze effect, that is, the changes in the hydrodynamics of a compound vegetated channel as a result of a decreased floodplain width was analyzed.

#### 3.1. Role of Vegetation

The influence of vegetation on decreasing the flow inside the floodplain can be clearly recognized. In the cases of a nonvegetated floodplain channel (Figure 4a), the velocity profiles can be divided into three main

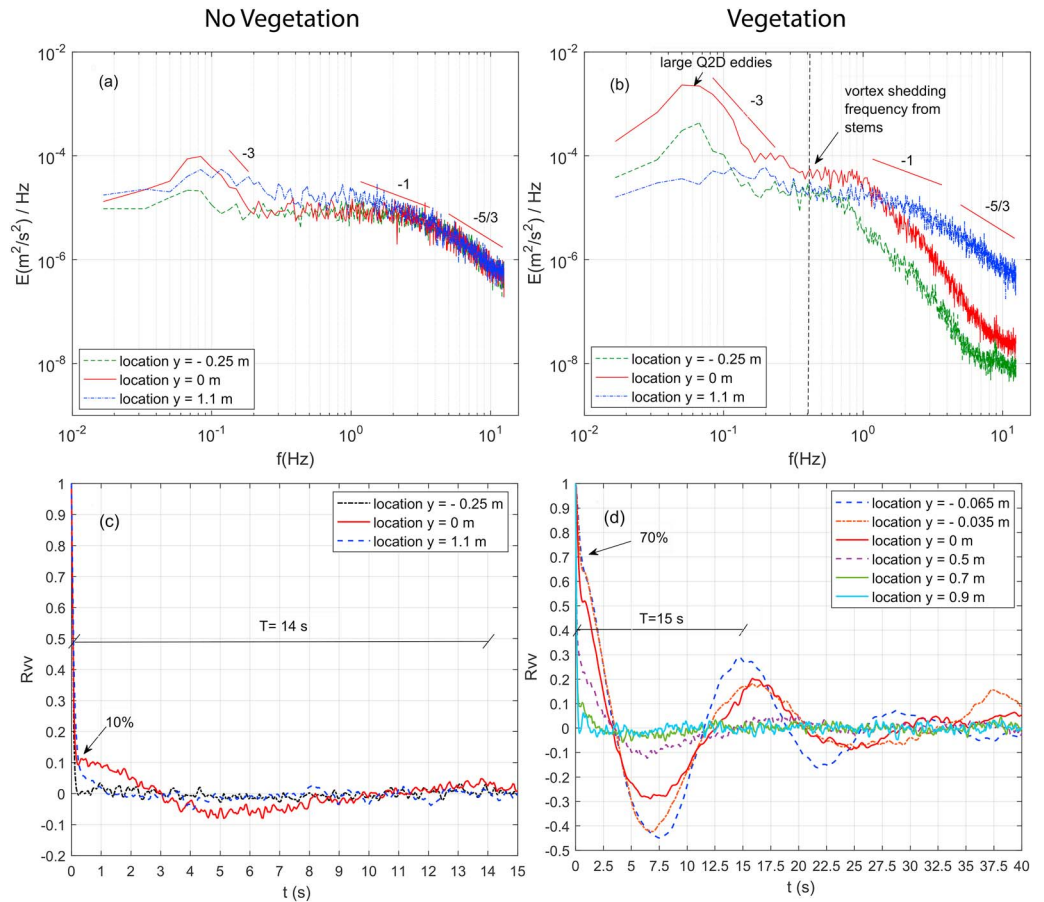


**Figure 5.** Power density spectra of lateral velocity fluctuations (a, b) and autocorrelation function  $R_{vw}$  (c, d) and at different locations from the wall;  $y = -0.25$  m located inside the vegetation,  $y = 0$  m located at the vegetated floodplain edge,  $y = 1.1$  m located outside in the main channel; (a, c) no vegetation, (b, d) dense vegetation; 50 cm width, discharge = 45 L/s, water level = 12 cm.

regions closely corresponding to their water depths, which are the floodplain area (from  $y = -0.5$  to  $0$  m), the main channel (from  $y = 0.8$  to  $1.5$  m), and the transition area (from  $y = 0$  to  $0.8$  m).

In all cases with a  $0.5$  m floodplain width, from the main channel toward the floodplain, the mean streamwise velocity gradually reduces over the transition slope region. Laterally uniform values of the mean streamwise velocity are presented right at the floodplain edge (location  $y = 0$  m in Figure 4a). This implies that the penetration of the main stream momentum into the floodplain region is zero. As the discharge and water depth increase, the mean streamwise velocity increases substantially. However, the penetration of the mixing layer into the floodplain region does not increase and the velocity gradient remains almost the same. With vegetated floodplain channels (Figure 4b), it is observed that the presence of cylinders boosts the magnitude of the velocity gradient about four times, from around  $0.2 \text{ s}^{-1}$  in scenarios without vegetation to  $0.8 \text{ s}^{-1}$  in scenarios with vegetation. Furthermore, the mean streamwise velocity suddenly decreases significantly in the middle of the transition slope ( $y = 0.4$  m) instead of gradually decreasing, in accordance with the transition slope (from  $y = 0.8$  to  $0$  m) as in the cases without vegetation. Also, a penetration of the shear layer into the cylinder arrays of about  $0.1$  m can be observed through the lateral distribution of the mean streamwise velocity. Furthermore, although the velocity gradient across the vegetated floodplain edge increases with the increase of the discharge, the mean streamwise velocity and the penetration of the shear layer into the canopy remain unchanged. Solely in the regions where there are no cylinders, including transition slope and main channel, the mean streamwise velocity was significantly affected.

Figures 4c and 4d show the transverse profiles of the RSs ( $-\overline{u'v'}$ ) in different scenarios with and without the cylinders. The positive values of the RSs indicate that the momentum is transferred toward the floodplain area. Increasing the input discharge  $Q$  and water level  $H$  does increase the RSs. In cases without vegetation,

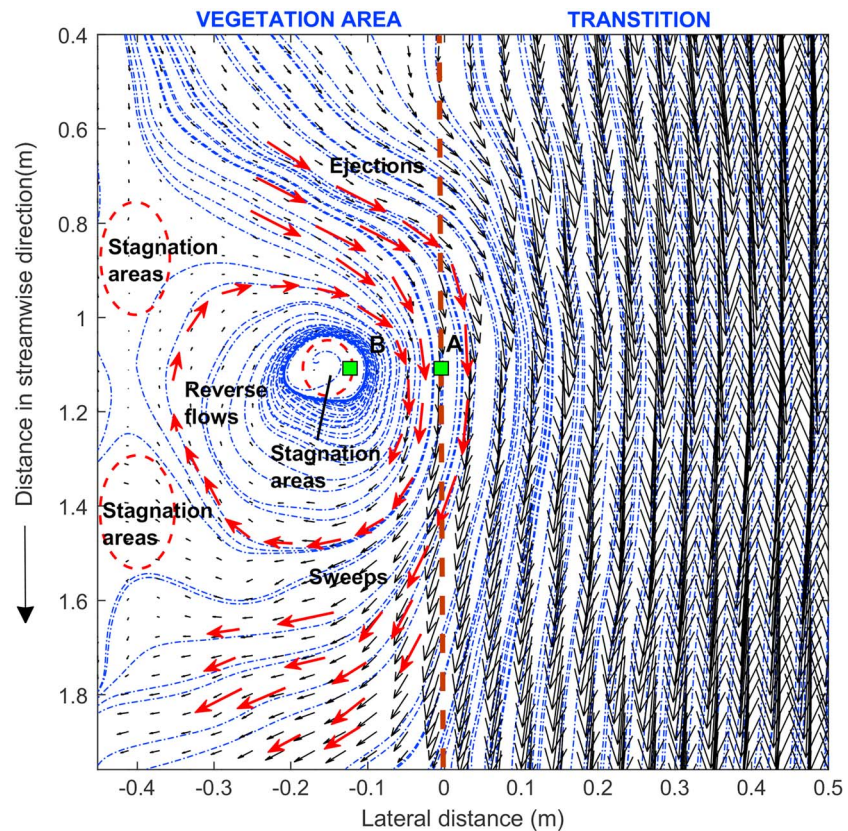


**Figure 6.** Representative ejections, sweeps, stagnation areas, and reverse flows captured in instantaneous velocity field at free surface measured by Particle Image Velocimetry (black arrows), case of dense density, 50 cm width, discharge  $Q$ : 45 L/s, water level  $H$ : 12 cm ( $y < 0$  indicates regions inside vegetated floodplain). The red arrows and the indicated stagnation areas illustrate experimental observations inferred from the instantaneous streamlines (blue dashed-dotted lines) of the instantaneous flow field.

the maximum values of RSs are located around the middle ( $y = 0.4$  m) of the transition region (from  $y = 0$  to 0.8 m). This means that the momentum exchange happens mostly at this location. However, in cases with vegetation, the maximum value of RSs significantly shifts toward the vegetation edge (location  $y = 0$  m). The results also show that the magnitude of the RSs in the cases without vegetation is quite small relative to that in cases with vegetation, by an order of magnitude. This demonstrates the role of vegetation in drawing greater momentum flux toward the floodplain vegetation region.

The presence of the LHCSs at the channel-vegetation interface and the influences of vegetation on their characteristics can be clearly identified in the power density spectra of the lateral velocity fluctuations  $v'$  at different locations along the cross-section (Figure 5). The results suggest that in cases without and with vegetation, there is a definite peak region in the power density spectrum, typically in the range of 0.05 to 0.1 Hz, corresponding to a fluctuation time scale of 10 to 20 s, but with much higher amplitude in the vegetated cases. The high-frequency side of the peak has a slope of approximately  $-3$  indicating the large turbulence structures possess two-dimensional characteristics (Uijttewaal & Booij, 2000). The energy density then seems to follow a  $-1$  slope character (Nikora, 1999; Perry & Li, 1990), which indicates that the large structures no longer possess the two-dimensional characteristic but sense the effect of the bottom friction.

Figures 5c and 5d show the representative profiles of the autocorrelation functions of the transverse velocity signals at different locations in cases without and with vegetation, respectively. In cases with vegetation (Figure 5d), it can be seen that at first the autocorrelation function decreases sharply down to 0.7, representing the smaller, three-dimensional scales in the turbulence spectrum. Then, the correlation falls off slower and its amplitude extrapolated to  $t = 0$  indicates that the large coherent structures contribute about 60–70% to the total normalized turbulent kinetic energy. Nevertheless, in cases without the vegetation (Figure 5c), it is seen that quasi-two-dimensional structures contribute only to about 10% of the total energy as the

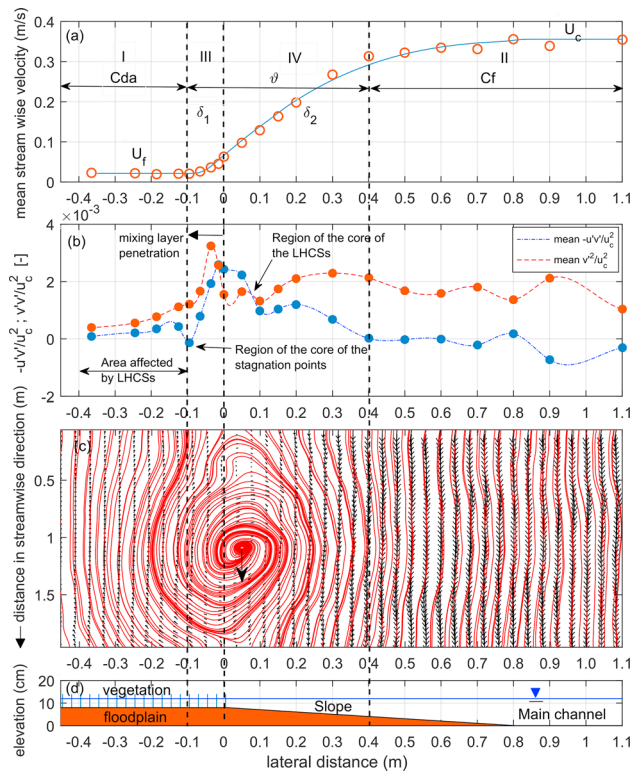


**Figure 7.** Representative Mean streamwise velocity in cases with vegetation (a). Representative comparison between the normal and shear stresses in the vegetated compound channel induced by the LHCSs (b). The representative LHCSs captured through the streamlines of the instantaneous fluctuating velocity field and its corresponding effect on the mean streamwise velocity (c). Dense scenario, 50 cm floodplain width, discharge = 45 L/s, water depth = 12 cm. LHCS = large horizontal coherent structure.

autocorrelation function at the floodplain edge decreases faster to around 0.1 after 0.1 s. Furthermore, the auto correlation modulation, which is related to the appearance of the LHCSs (Uijtewaal & Booij, 2000) is much weaker in cases without vegetation compared to cases with vegetation. This confirms that the LHCSs in cases with dense vegetation are stronger, more pronounced, and contain more energy than in cases without vegetation. Moreover, the difference in the appearance of the LHCSs in scenarios with and without vegetation implies that in the current experiment, for conditions tested, the presence of vegetation appears to be the dominant factor controlling the dynamics of the mixing layer, rather than the depth differential associated with the floodplain.

### 3.2. Role of LHCS

In order to get an insight into how the LHCSs affect the flow field, it is necessary to understand the movement of the structures themselves. Although it is not always straightforward to visualize the LHCSs by simply looking at the velocity vector field in the PIV data set, the motion of the LHCSs along the vegetation interface leaves an important trace, which is the presence of stagnation areas moving along together with the LHCSs. Capturing these stagnation areas and their movement within the vegetated floodplain area in the instantaneous velocity field (Figure 6) reveals a cycloid motion.

As the large coherent structures move along the interface between cylinder arrays and the open channel, they create inflows, which we term sweeps ( $u' > 0, v' < 0$ ). In the beginning, the sweeps accelerate outside the vegetation as the depth decreases in the transverse direction. However, when the sweeps enter the vegetation regions, due to the surrounding slow flow and the drag forces of the vegetation, they are strongly disturbed and decelerated significantly, even become stagnant and reverse direction before flowing out from the cylinder arrays through the ejection events at the end of the cycle. It is also observed that the regions where the flows are almost stagnant ( $u, v \sim 0$ ), which are termed stagnation areas, are found along the streamwise direction next to the LHCSs.

The transverse velocity is hindered by the vegetation and the vertical wall which according to the Bernoulli's principle lead to the elevated free surface at the stagnation points. This drives the reverse flows as this

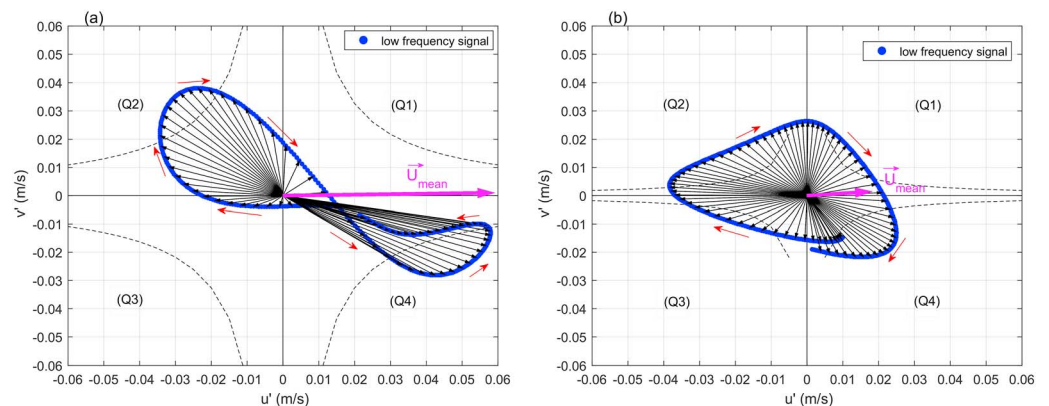


**Figure 8.** The representative motion (red arrows) of the quadrant analysis of the horizontal fluctuations associated with low-frequency signal (blue circles) in a period of 15 s, location A at the edge of vegetated floodplain ( $y = 0$  m) (a) and location B at  $y = -0.125$  m inside the vegetation (b). Black arrows indicate the instantaneous fluctuation velocity; the pink arrows indicate the mean flow velocity at those locations. The dashed lines in the figure represent hyperbolas corresponding to  $|u'v'| = 2(-u'v')$ .

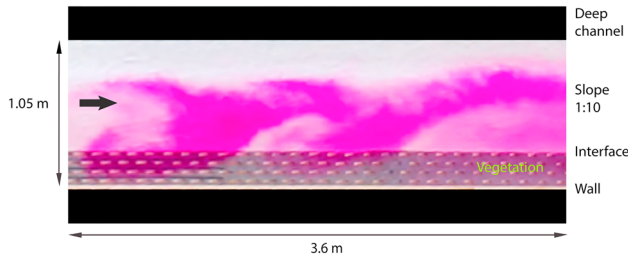


**Figure 9.** Cycloid Flow field under the effect of the large horizontal coherent structures visualized by the color dye for sparse density scenarios and, respectively, 25 cm floodplain width. The large horizontal coherent structures as it moves along the cylinder arrays shows a “cycloid motion” property.

induced pressure gradient apparently larger than the mean gradient from water slope. Further away from the stagnation areas, as this pressure becomes weaker, the reverse flow becomes weaker and its interaction with the streamwise flow creates other stagnation areas. In this way, the surrounding areas where the flow induced by the increased local pressure can reach are also affected by the LHCSs. Hence, the transverse distance affected by the LHCSs is larger than the distance in which the mean profile of the mixing layer can penetrate. Figure 6 confirms these analyses. It can be seen that the vegetation area affected by the LHCSs is of the size of around 0.35–0.4 m which is about four times larger than the distance over which the mean streamwise velocity profile achieves its constant value (about 0.1 m; Figure 4b).

Furthermore, it is noted that as the LHCSs move, they cause velocity fluctuations resulting in the fluctuation of the forces on the stems (see Figure A2 in the appendix). The fluctuations are strongest at the floodplain edge and become weaker further inside the vegetation. Negative values of the streamwise forces can also be clearly observed. These negative values caused by the stagnant and reverse flow events are not observed at the edge of floodplain. In this context, it is suggested that the sweep and ejection events appear to dominate the edge region of vegetation, while the stagnation areas and reverse flows are likely to occur further into the vegetated region.

The influences of LHCSs on the flow inside the vegetation can remain significant even when there is an insignificant amount of momentum exchange induced by the LHCSs. While the former is related to the lateral fluctuation velocity  $v'$  and thereby is proportional to the normal stresses  $-\overline{v'v'}$ , the latter is proportional to the RSs ( $RSs = -\overline{u'v'}$ ). A comparison between these two stresses (Figure 7b), along with the results of Figure 6 demonstrate that the region inside the vegetation affected by the LHCSs can be much larger than the area where the transverse momentum exchange induced by LHCSs can occur.

Studying the quadrant analysis of the RSs at two different locations A and B (see Figure 6) makes it possible to understand how the stagnation areas and reverse flow events can occur and why they are barely observed in the literature. Figure 8 shows a quadrant analysis in a period of 15 s of the horizontal fluctuations associated with low-frequency signal (blue circles), which correspond to the LHCSs at the edge of the vegetated floodplain (location A:  $y = 0$  m) and inside the vegetation (location B:  $y = -0.125$  m). Although the stagnation areas and reverse flow events observed in the flow field do not directly appear in quadrant analysis of the RSs ( $u', v'$ ), these flow events can be recognized by adding in the quadrant analysis the mean flow velocity (pink arrows) together with instantaneous fluctuation velocities (in the form of vectors) corresponding to the distribution of ( $u', v'$ ) in time (black arrows). It is noted that the phase relation between  $u'$  and  $v'$  is different for both locations. In this way, there are two main components in the quadrant analysis of the RSs, the fluctuation motion caused by the LHCSs and the mean flow motion caused by the mean free surface

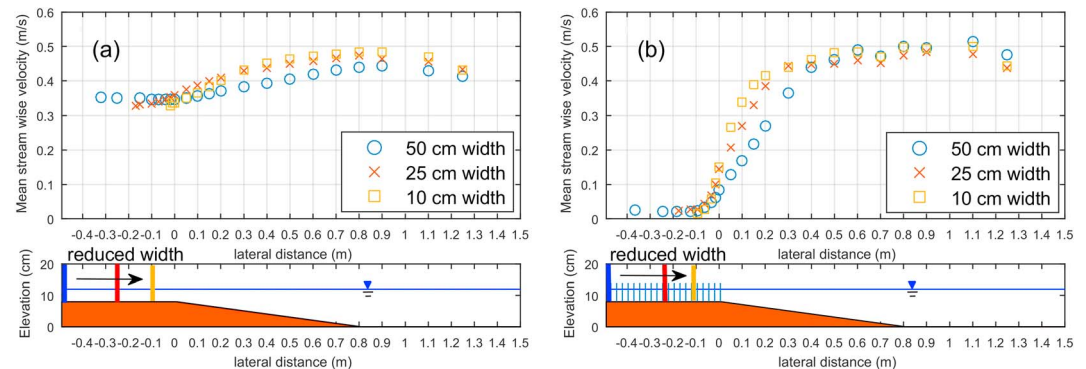


**Figure 10.** Mean streamwise velocity profile in nonvegetated floodplain scenarios and dense vegetation scenarios, discharge  $Q = 80$  L/s, water level  $H = 14$  cm, different floodplain widths—circles = 50 cm; crosses = 25 cm; squares = 10 cm.

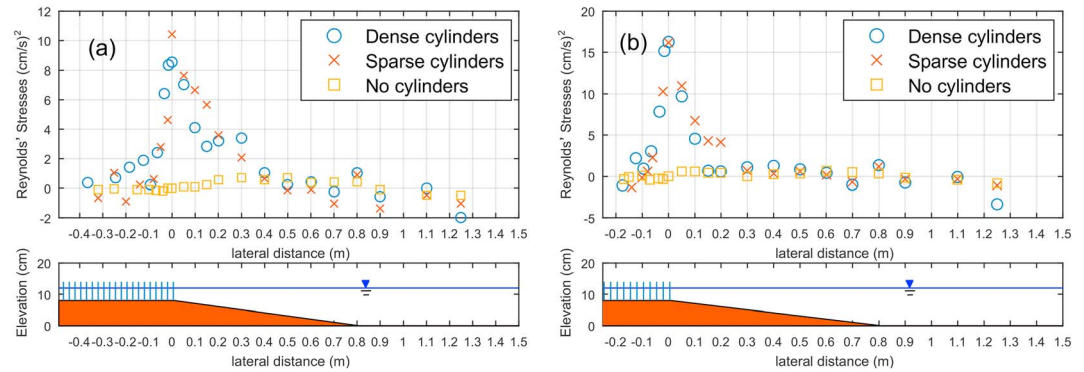


**Figure 11.** Lateral profiles of Reynold stress in case of 50 cm floodplain width (a) and 25 cm floodplain width (b); no cylinder (squares), sparse cylinder (crosses), and dense cylinders (circles); discharge  $Q = 80$  L/s, water level  $H = 12$  cm.

water slope. The essential conditions so that the stagnation areas or reverse flow events can occur can be stated as follows:

“the LHCSs need to be strong enough, and the mean flow velocity needs to be small enough so that the fluctuation motions induced by the LHCSs become equal or larger than the mean flow velocity.”

The observation suggests that the tracer path of the dye follows a prolate cycloid curve (Figure 9). The observations confirm the presence of the LHCSs and the flow events caused by the motion of the LHCSs along the vegetated floodplain.

The LHCSs then can be identified by subtracting the advection velocity at the center of the stagnation areas from the instantaneous velocity field (Figure 7c). It is shown that when moving along the interface, the LHCSs clearly split the mean streamwise velocity into three different regions (Figure 7a) the uniform region inside the floodplain (region I) controlled by the drag from vegetation, outside in the main channel (region II) controlled by the bottom friction and water depth, and the mixing layer region (regions III and IV). These results suggest that in a compound vegetated channel with a very gentle slope, for the conditions tested ( $\frac{C_d a}{C_f / D} \geq 60$ ), the vegetated shear layer dynamics resembled to that associated with vegetation alone, as described in White and Nepf (2007, 2008), rather than that associated only with a depth differential.

### 3.3. Role of Vegetation Width or Squeeze Effect

Finally, the squeeze effect (Truong et al., 2017) has been experimentally studied by varying the width of the floodplain region. Figure 10 shows the mean streamwise velocity for different floodplain widths. It is shown

that the width of the floodplain does affect the penetration of the mixing layer into the floodplain area. In cases without vegetation, 50 cm floodplain width (Figure 10a), the mean streamwise velocity achieved uniform values of 34.9 cm/s right at the floodplain edge ( $y = 0$  m). When reducing the width of the floodplain from 50 to 25 cm and 10 cm, the mean streamwise velocity does not achieve a transverse uniform value at the floodplain edge and keeps decreasing further inside the floodplain region. This means that the penetration of the mixing layer increases together with the decrease of the width of the floodplain.

In the case of dense vegetation (Figure 10b), the response of mean streamwise velocity within the floodplain region is less sensitive. As the width of the floodplain reduces from 50 to 25 cm, the mean streamwise velocity shows different trends only in the outer region (from location  $y = 0$  to around  $y = 0.5$  m) where the velocity gradient significantly increases. This means that the velocity gradient around the vegetation interface can be increased by decreasing the floodplain width. These changes in the velocity can be explained in terms of the increased velocity gradient at the vegetated edge which was induced by the changes in the pattern of the LHCSs.

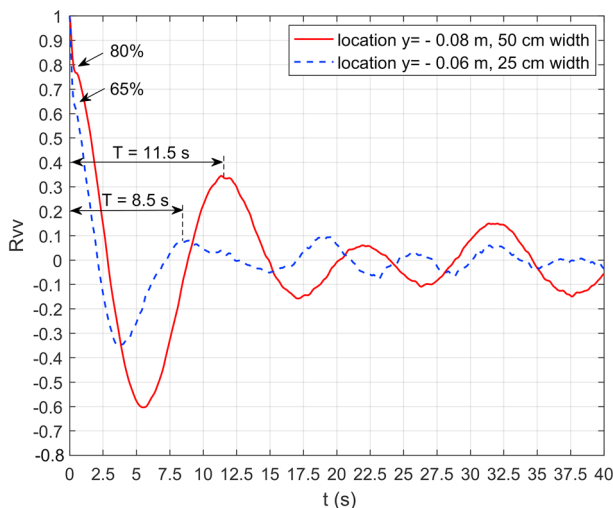


**Figure 12.** Autocorrelation function  $R_{vv}$  in cases of sparse density, floodplain width = 50 and 25 cm; discharge  $Q = 45$  L/s, water level  $H = 12$  cm.

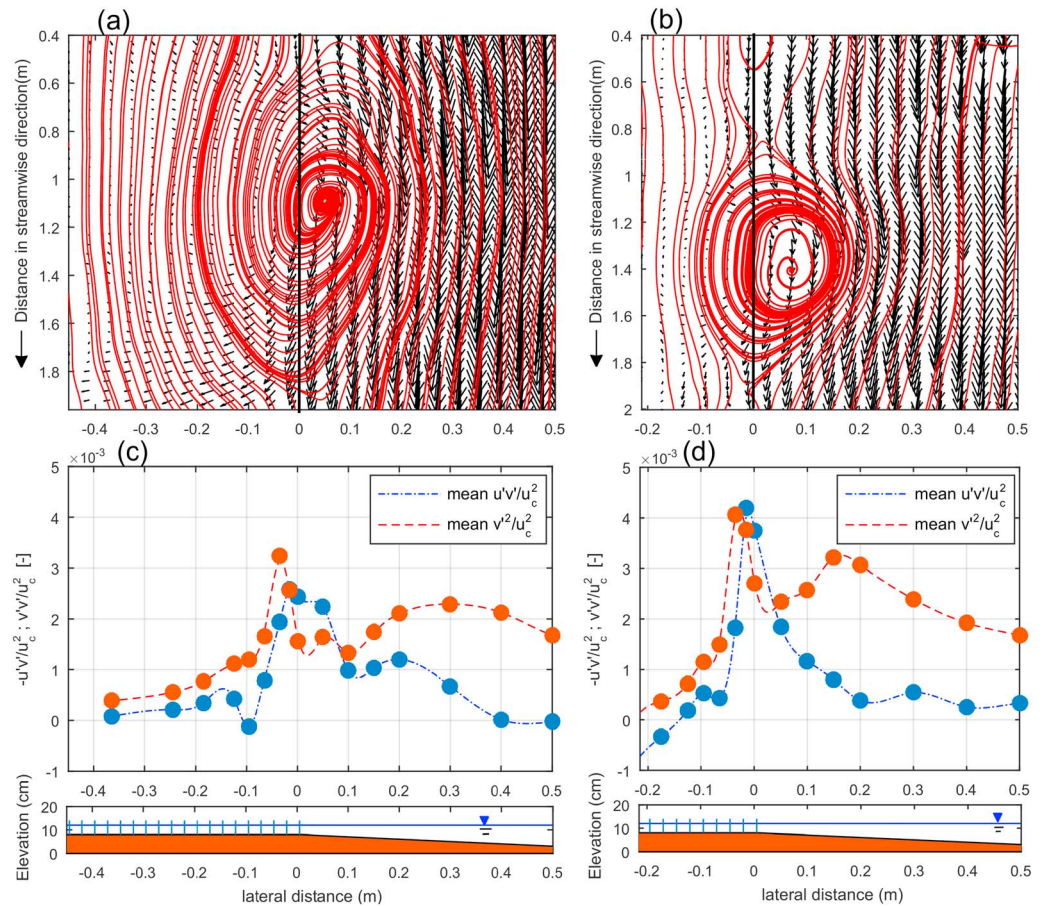


**Figure 13.** The Large Horizontal coherent structure (red-solid lines) in cases of 50 cm width (a) and 25 cm width (b) and the corresponding shear and normal stresses in cases of 50 cm width (c) and 25 cm width (d). Dense scenarios, discharge = 45 L/s, water level = 12 cm.

It can be seen that the increased velocity gradient together with the presence of vegetation does not lead to a larger penetration of the shear layer into the vegetated floodplain. In both cases (50 and 25 cm floodplain width), the mean streamwise velocity decreases inside the floodplain region and achieves a transversely uniform value beyond about 10 cm penetration. This indicates that the mean streamwise velocity does require a certain distance such that a transversely uniform velocity within the forest can be achieved. In these scenarios, the distance required is about 10 cm. Differences can be noted when further reducing the width of the floodplain from 25 to 10 cm, the mean streamwise velocity within the vegetated floodplain starts “feeling” the side wall and is being affected. The mean streamwise velocity cannot achieved a transverse uniform value as it keeps decreasing until the end of the floodplain region. This means that the mixing layer appears to penetrate the whole floodplain region.

Figure 11a shows the transverse profiles of the RSs in cases of different density and different width. Although strong peaks of RSs can be clearly observed in cases with the presence of cylinders (sparse and dense scenarios), in cases without vegetation, it is less obvious as the maximum values tend to spread more along the transition slope region. It is also observed that the more vegetation, the less spreading of the RSs. When the width of the floodplain is reduced to 25 cm (Figure 11b), the RSs around the floodplain edge (location  $y = 0$  m) increase. As the order of magnitude of the RSs is related to the momentum exchange in the mixing layer, this implies an increase in the momentum exchange between these two regions when the floodplain width is restricted.

The autocorrelation functions of lateral velocity in different floodplain width scenarios are shown in Figure 12. Reducing the width of the floodplain also reduces the period of the quasi-2-D structure, from 11.5 to 8.5 s. Besides, the normalized energy contribution also reduces from 80% to 65%. These results

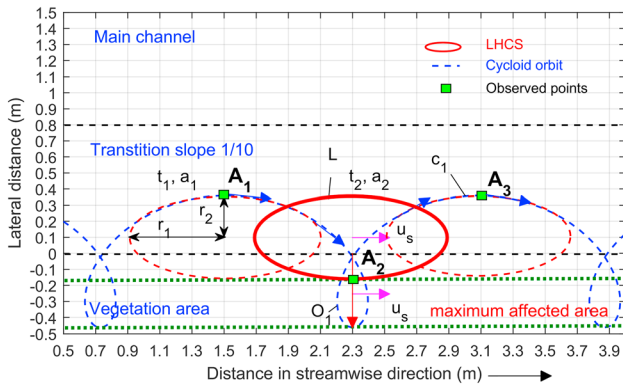


**Figure 14.** Schematic view of cycloid motion under the effect of the LHCSs as they are moving along the vegetated interface. The maximum affected area is larger than the penetration of the LHCSs. LHCS = large horizontal coherent structure.

show that squeezing the floodplain does increase the frequency of the LHCSs. This is probably due to the smaller LHCSs and faster advection velocity. In terms of Kelvin-Helmholtz instability, the results suggest that decreasing the floodplain width results in a smaller wavelength and wave period. The results of Figures 13a and 13b confirm this.

Finally, the response of the structures themselves to the “squeeze effect” is addressed. Figure 13a shows the representative LHCSs (solid red lines) in cases of 50 cm floodplain width. The corresponding LHCSs in cases where the width of vegetated floodplain has been reduced to 25 cm is shown in Figure 13b. It can be seen that the LHCSs are smaller in the streamwise and lateral direction in the narrower floodplain scenarios of a so-called squeezed condition.

The combined impact of the LHCSs and the narrower space of the floodplain area may cause a stronger increase in the local pressure, associated with the stagnation areas and reverse flows. As a result, the reverse flow and the RSs in the vegetation region in cases of the narrower 25 cm floodplain width are larger than that in the scenario of 50 cm floodplain width (Figures 13c and 13d). Additionally, the more frequent LHCSs means that the flow events occur more rapidly and region of stagnation areas move faster. In this sense, sedimentation processes may be significantly affected in such a way that there is less time and space for the sediment to be deposited, while the momentum fluxes are larger.

#### 4. Discussion

The results of our work were based on a laboratory experiment of a vegetated compound channel mimicking estuarine mangroves. The dense vegetation scenarios in the experiment are representative for sparse cases of mangroves in reality. It is noted that the roots and stems of mangroves are rigid, which are different from flexible plants such as saltmarshes. The experimental results indicate that vegetation, in general, and mangroves, in particular, have a strong role in determining the strength and direction of flow in river channels with vegetated floodplains. Large differences in the mean streamwise velocity and RSs between the scenarios with and without vegetation can be observed. It is important to note that these differences are not only caused directly by the presence of vegetation in the floodplain region (i.e., vegetation disturbs, diverts, and reduces the flow velocities), but also due to the presence of the LHCSs, generated by the vegetation-induced shear layer. Therefore, differences were observed to occur not only at the vegetation interface, but also deeper inside the vegetation area, and in the adjacent transition slope. The phenomenon in which areas deeper inside the vegetation, or outside in the transition slope, are affected by the flow events generated by LHCSs as they move along the vegetation interface can be conceptually explained through the cycloid characteristic of the flow field (Figure 14).

Based on the observation of the particle movement in the PIV data set and the previous analyses, it is seen that the LHCSs (L) in this case have the ellipsoidal form with two radii corresponding to the length  $r_1 =$

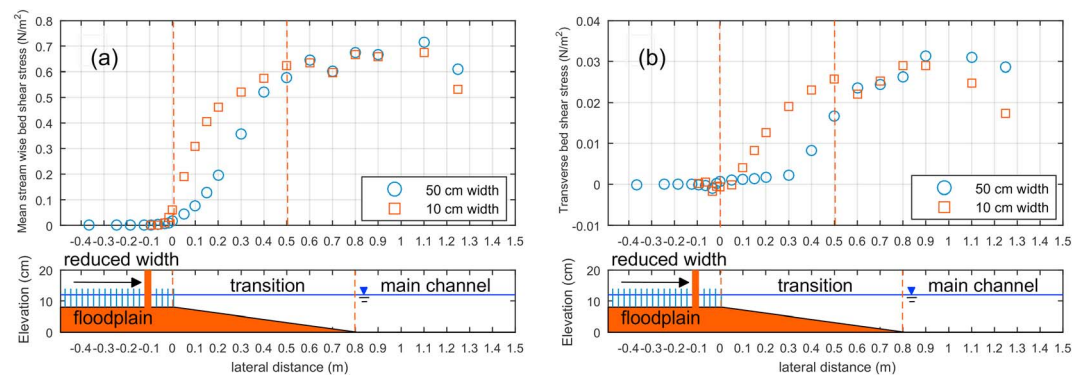


**Figure 15.** Streamwise bed shear stress comparison (a) and transverse bed shear stress comparison (b) in scenarios of 50 and 10 cm floodplain width, discharge  $Q = 80$  L/s, water level  $H = 14$  cm. The positive values of the transverse bed shear stress indicate that it is directed away from the floodplain.

0.6 m, and to the width  $r_2 = 0.25$  m. At the moment  $t_1$ , the LHCSs is at location  $a_1$ , and an observed point  $A_1$  located at its edge tends to follow the orbit of a prolate cycloid curve  $c_1$ . At the moment  $t_2$ , the LHCSs is at location  $a_2$ , and an observed point  $A_1$  follows the orbit of a prolate cycloid curve  $c_1$  to the location  $A_2$ . In the vegetation region outside the mixing layer, areas surrounding the prolate cycloid curve  $c_1$  appear to be affected by the motion of the LHCSs and tend to follow the motions of the observed point (A1-A2-A3). This results in a stagnant area. As the LHCSs are moving along the interface between vegetation and open region, these stagnation areas also move with the same velocity  $u_s$ . In this sense, the region of the stagnation area captured by PIV measurement is likely to link to the cycloid loop ( $O_1$ ) at the time  $t_2$ . The corresponding LHCSs at this moment at location  $a_2$  can be deduced by subtracting the instantaneous velocity field to the advection velocity  $u_s$  at the center of stagnation areas ( $O_1$ ). According to this explanation, it is suggested that the maximum affected area is likely to connect to the width of the outer layer of the LHCSs. In practical engineering, this means that a structure which directly interferes with the vegetated river bank should be carefully considered, especially in terms of the changes of the hydrodynamics and exchange processes induced by the modification of the LHCSs. It could be interesting to analyze the combination of structured large-scale motion and irregular small-scale motion in terms of Kolmogorov complexity to see the analogy with other self-organizing flows (Mihailovic et al., 2017), but this lies outside of the scope of this research.

It is noted that a similar phenomenon of the interaction of the LHCSs and cylinder arrays was described by White and Nepf (2007), but in terms of the phase difference between  $u'$  and  $v'$ . The interaction of the LHCSs and stagnation points inside the vegetation region discussed in this study is related to the Lagrangian coordinate system. Hence, the latter provides a different view on the phenomenon. For example, it is worth noting that while the effects of the sweeps and ejections have been well recognized (Wallace, 2016; White & Nepf, 2007), the reverse flow and stagnation areas inside vegetation region have not been observed in cases with a flat bed. The presence of a transverse slope appears to play an important role in this behavior, see, for example, van Prooijen et al. (2005). It is seen from the experiment that the reverse flow and stagnation areas inside the vegetation region are relevant factors potentially affecting the sedimentation and nutrient deposition within the cylinder arrays.

The stability of the river bank in squeezed condition, that is, the mangrove width is restricted, is discussed here in terms of the changes in the bed shear stress. The total bed shear stress  $\tau_b$  is composed of transverse bed shear stress  $\tau_{bt} = \rho C_f UV$  and streamwise bed shear stress  $\tau_{bs} = \rho C_f U^2$ :

$$|\tau_b| = \sqrt{(\rho C_f U^2)^2 + (\rho C_f UV)^2}. \quad (1)$$

The secondary circulations is assumed small and can be neglected,  $\rho$  is the density of water,  $C_f$  is bottom friction coefficient,  $U$  and  $V$  are the depth averaged velocity in streamwise and lateral direction.

Based on the results of the experiment, the bed shear stresses, which are representative for the applied forces induced by the flow, including the LHCSs can be determined (Figure 15). It can clearly be seen that, when the mangrove width is reduced, although the bed shear stress in the inner layer remains almost the same, the bed shear stress in the outer layer (both streamwise and transverse) increases significantly.

The outer layer appears to be the most sensitive area in terms of bed shear stresses. Significant variation in the bed shear stresses induced by changes in the LHCSs can be expected when decreasing the forest width. Consequently, changes in applied bed shear stresses to the river bank may cause variations in the bed erosion rate modeled by the excess stress equation of Partheniades (1965). Therefore, the width of the vegetation area does play a role in the stabilization of a vegetation compound channel, especially for the transition slope. Reducing the width of the vegetation may increase the applied bed shear stresses on the transition slope, causing the instability of the vegetated floodplain. As far as practical engineering is concerned, these results imply that there should be a minimum width required for the sustainable development of a vegetated floodplain.

## 5. Conclusions

The effect of vegetation on the hydrodynamics of a compound channel, the presence of the LHCSs, and their effects on the flow field as well as “squeeze” effects were investigated through experiments. It is shown that in a compound vegetated channel with a gentle transverse slope, the shear layer properties are dominated by the presence of vegetation, rather than by the water depth difference. The vegetation significantly

increases the gradient of the mean streamwise velocity, drawing more exchange toward the vegetation edge and pushing more flow into the floodplain region. It is also very effective in damping and shielding the flow within the forest from external boundary conditions. Furthermore, the presence of vegetation does enhance the occurrence of LHCSs, which is a dominant factor in forcing the exchange mechanism at the vegetation interface. The presence of LHCSs, which is much more pronounced in cases with vegetation, is the major factor contributing to the momentum exchange between the vegetated floodplain regions and the adjacent open channel. The experimental results also reveal that the region affected by the LHCSs where large transverse fluctuations can occur is much larger than the region of transverse momentum exchange which is connected to the penetration of the LHCSs into the vegetated floodplain region. The moving of the LHCSs along the vegetation interface is associated with the sweeps, the ejections, as well as the stagnant and the reverse flows forming a so-called cycloid motion. While the sweeps and ejections dominate the momentum exchange region and appear to link to the import and export mechanism of nutrients and sediments, the stagnant and reverse flows appear to dominate the region further inside the vegetation and are important for the deposition processes. The streamwise force is maximum during the sweeps and smallest during the ejections. Moreover, due to the presence of stagnant and reverse flows, negative streamwise forces can be recorded.

It is important to note that although the vegetation is very effective in damping and prohibiting the hydrodynamic impacts within the forest, the squeeze effect makes this protection much less successful. Reducing the forest width does influence the hydrodynamics in and around the cylinder arrays, especially the shear layer at the vegetation interface. Furthermore, the mean flow velocity needs a certain space to reach its uniform value inside the floodplain area and the vegetated region affected by the LHCSs can be even larger than the region which the mixing layer can penetrate into. Hence, a too narrow floodplain may diminish the affected area directly and makes it impossible for the flow field inside the vegetation to be able to reach its equilibrium state. As a result, the LHCSs in squeeze condition occur more frequently, but less regularly and the transverse exchange processes induced by these LHCSs can be strongly disturbed. The momentum fluxes are larger, and the time and space for the sediment to be deposited is restricted. These are hypothesized to not create favorable conditions for the nutrient or sediment deposition within the forest. It is also seen that the denser the vegetation, the less sensitive the mangrove forest is to the squeeze effects. This again shows the vegetation function in the protection of the river banks.

## Appendix A

### A1. Experiment Setup and Results

The velocity was measured using an Acoustic Doppler Velocity (ADV) at a sampling rate of 25 Hz. Velocity measurements were taken over a time interval of 10 min in order to achieve representative statistical data. Besides, in order to obtain a good particle seeding in the flowing water, an electrolyzer with 0.1 mm thick

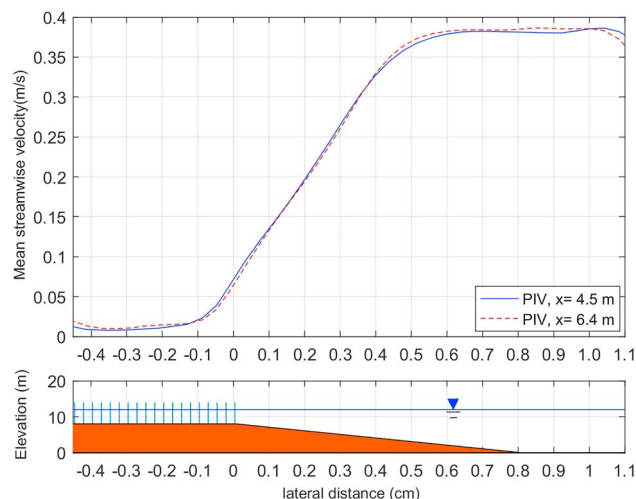


**Figure A1.** A representative comparison of mean streamwise velocity measured from Particle Image Velocimetry between locations  $x = 4.5$  m and  $x = 6.4$  m.

**Table A1**  
A Comparison of the Vegetation Drag

|                               | White and Nepf (2007) |        | Current study |       |
|-------------------------------|-----------------------|--------|---------------|-------|
| $\Phi$                        | 0.02                  | 0.045  | 0.01          | 0.04  |
| $N(\text{number}/\text{m}^2)$ | 603                   | 1356   | 137           | 550   |
| $d(\text{m})$                 | 0.0065                | 0.0065 | 0.01          | 0.01  |
| $Cda_{\text{theory}}$         | 0.039                 | 0.088  | 0.014         | 0.056 |
| $Cda_{\text{measured}}$       | 0.092                 | 0.285  | 0.029         | 0.094 |
| $Cda_{ U Ux}$                 | -                     | -      | 0.023         | 0.049 |

**Table A2**  
Experimental Configuration and Major Results

| Cases                         | An1   | An2   | An3   | An4   | Bn1   | Bn2   | Bn3   | Bn4   | As1   | As2   | As3   | As4   | Bs1   | Bs2   | Bs3   | Bs4   |
|-------------------------------|-------|-------|-------|-------|-------|-------|-------|-------|-------|-------|-------|-------|-------|-------|-------|-------|
| $N(\text{number}/\text{m}^2)$ | 0     | 0     | 0     | 0     | 0     | 0     | 0     | 0     | 139   | 139   | 139   | 139   | 139   | 139   | 139   | 139   |
| $\Phi$                        | 0     | 0     | 0     | 0     | 0     | 0     | 0     | 0     | 0     | 0     | 0     | 0     | 0.01  | 0.01  | 0.01  | 0.01  |
| $C_D \cdot a$ (cm/s)          | 0     | 0     | 0     | 0     | 0     | 0     | 0.0   | 0.029 | 0.025 | 0.028 | 0.027 | 0.019 | 0.019 | 0.017 | 0.019 |       |
| Width (cm)                    | 50    | 50    | 50    | 50    | 25    | 25    | 25    | 25    | 50    | 50    | 50    | 50    | 25    | 25    | 25    | 25    |
| $Q$ (L/s)                     | 45    | 60    | 80    | 80    | 45    | 60    | 80    | 80    | 45    | 60    | 80    | 80    | 45    | 60    | 80    | 80    |
| $D_f$ (cm)                    | 3.90  | 4.84  | 6.26  | 4.40  | 4.13  | 5.12  | 6.47  | 4.11  | 4.76  | 5.17  | 6.47  | 4.59  | 4.82  | 5.59  | 6.28  | 4.66  |
| $D_c$ (cm)                    | 11.90 | 12.84 | 14.26 | 12.40 | 12.13 | 13.12 | 14.47 | 12.11 | 12.76 | 13.17 | 14.47 | 12.59 | 12.82 | 13.59 | 14.28 | 12.66 |
| $Dr = D_f/D_c$                | 0.33  | 0.38  | 0.44  | 0.35  | 0.34  | 0.39  | 0.45  | 0.34  | 0.37  | 0.39  | 0.45  | 0.36  | 0.38  | 0.41  | 0.44  | 0.37  |
| $Fr$                          | 0.33  | 0.41  | 0.44  | 0.58  | 0.32  | 0.38  | 0.41  | 0.59  | 0.29  | 0.36  | 0.4   | 0.5   | 0.27  | 0.32  | 0.39  | 0.47  |
| $R_{ec} (\times 10^3)$        | 39.83 | 49.55 | 61.57 | 62.05 | 39.93 | 51.23 | 65.30 | 64.87 | 41.03 | 53.53 | 69.09 | 69.49 | 38.87 | 49.79 | 66.0  | 65.95 |
| $R_{ef} (\times 10^3)$        | 8.02  | 13.64 | 21.81 | 16.70 | 8.32  | 13.62 | 21.38 | 15.29 | 2.27  | 3.57  | 4.86  | 4.63  | 2.30  | 3.35  | 4.60  | 4.28  |
| $U_f$ (cm/s)                  | 20.9  | 28.2  | 34.9  | 38    | 20.2  | 26.6  | 33.2  | 37.3  | 4.8   | 6.9   | 7.9   | 9.8   | 4     | 5.3   | 6.3   | 8.4   |
| $U_c$ (cm/s)                  | 33.5  | 39.8  | 44.4  | 51.5  | 34.9  | 41.3  | 47.4  | 56.3  | 33.3  | 42.1  | 49.6  | 56.9  | 33.2  | 40.3  | 50.3  | 56.5  |
| $U_s$ (cm/s)                  | 0     | 0     | 0     | 0     | 2.4   | 3     | 2.6   | 4.1   | 3.9   | 4.4   | 5.1   | 5.7   | 5.4   | 7     | 9.3   | 9.7   |
| Pene (cm) <sup>a</sup>        | 0     | 0     | 0     | 0     | 6.6   | 6.6   | 3     | 5.4   | 9.8   | 8.8   | 8.9   | 8.1   | 9.2   | 9.2   | 9.3   | 8.9   |
| Cases                         | Cs1   | Cs2   | Cs3   | Cs4   | Ad1   | Ad2   | Ad3   | Ad4   | Bd1   | Bd2   | Bd3   | Bd4   | Cd1   | Cd2   | Cd3   | Cd4   |
| $N(\text{number}/\text{m}^2)$ | 139   | 139   | 139   | 139   | 556   | 556   | 556   | 556   | 556   | 556   | 556   | 556   | 556   | 556   | 556   | 556   |
| $\Phi$                        | 0.01  | 0.01  | 0.01  | 0.01  | 0.04  | 0.04  | 0.04  | 0.04  | 0.04  | 0.04  | 0.04  | 0.04  | 0.04  | 0.04  | 0.04  | 0.04  |
| $C_D \cdot a$ (cm/s)          | 0.019 | 0.013 | 0.012 | 0.012 | 0.094 | 0.153 | 0.132 | 0.106 | 0.124 | 0.115 | 0.127 | 0.089 | 0.117 | 0.084 | 0.054 | 0.059 |
| Width (cm)                    | 10    | 10    | 10    | 10    | 50    | 50    | 50    | 50    | 25    | 25    | 25    | 25    | 10    | 10    | 10    | 10    |
| $Q$ (L/s)                     | 45    | 60    | 80    | 80    | 45    | 60    | 80    | 80    | 45    | 60    | 80    | 80    | 45    | 60    | 80    | 80    |
| $D_f$ (cm)                    | 4.40  | 5.11  | 6.49  | 4.44  | 4.22  | 5.21  | 6.42  | 4.64  | 4.33  | 5.43  | 6.74  | 4.53  | 4.47  | 5.75  | 6.49  | 4.47  |
| $D_c$ (cm)                    | 12.40 | 13.11 | 14.49 | 12.44 | 12.22 | 13.21 | 14.42 | 12.64 | 12.33 | 13.43 | 14.74 | 12.53 | 12.47 | 13.75 | 14.49 | 12.47 |
| $Dr = D_f/D_c$                | 0.35  | 0.39  | 0.45  | 0.36  | 0.35  | 0.39  | 0.44  | 0.37  | 0.35  | 0.40  | 0.46  | 0.36  | 0.36  | 0.42  | 0.45  | 0.36  |
| $Fr$                          | 0.26  | 0.32  | 0.35  | 0.45  | 0.31  | 0.36  | 0.42  | 0.52  | 0.29  | 0.33  | 0.36  | 0.47  | 0.31  | 0.34  | 0.41  | 0.51  |
| $R_{ec} (\times 10^3)$        | 34.92 | 47.36 | 61.23 | 62.30 | 41.40 | 53.70 | 71.48 | 72.83 | 39.42 | 51.30 | 64.41 | 64.98 | 42.37 | 53.75 | 70.10 | 71.03 |
| $R_{ef} (\times 10^3)$        | 2.83  | 4.38  | 6.69  | 5.59  | 0.90  | 1.03  | 1.39  | 1.70  | 0.95  | 1.42  | 1.79  | 2.01  | 1.83  | 3.02  | 4.62  | 3.44  |
| $U_f$ (cm/s)                  | 3.5   | 2.6   | 7.2   | 8.9   | 2.1   | 2.1   | 2.2   | 3.7   | 2.2   | 2.6   | 2.7   | 4.5   | 1     | 1     | 1.6   | 2.5   |
| $U_c$ (cm/s)                  | 34.2  | 42.5  | 49.6  | 58.4  | 35.6  | 41.9  | 51.5  | 58.7  | 34.9  | 41.2  | 48.3  | 58.5  | 35    | 40.2  | 50    | 59.3  |
| $U_s$ (cm/s)                  | 8.2   | 10.6  | 9.4   | 10.8  | 4.5   | 5.8   | 6.4   | 7.5   | 6.7   | 9     | 11.7  | 11.9  | 7.94  | 11    | 14.2  | 14.6  |
| Pene (cm)                     | 10    | 10    | 10    | 10    | 7.6   | 8.4   | 8.7   | 7     | 8.3   | 8.1   | 8.4   | 6.8   | 10    | 10    | 10    | 10    |

<sup>a</sup>Penetration (Pene) in this table is defined to be the distance from the position where the mean streamwise velocity is 5% different from the value of the uniform velocity inside the vegetated floodplain ( $U_{5\%} = U_f + 5\% \cdot U_f$ ) to the edge of the floodplain ( $y = 0$  m).

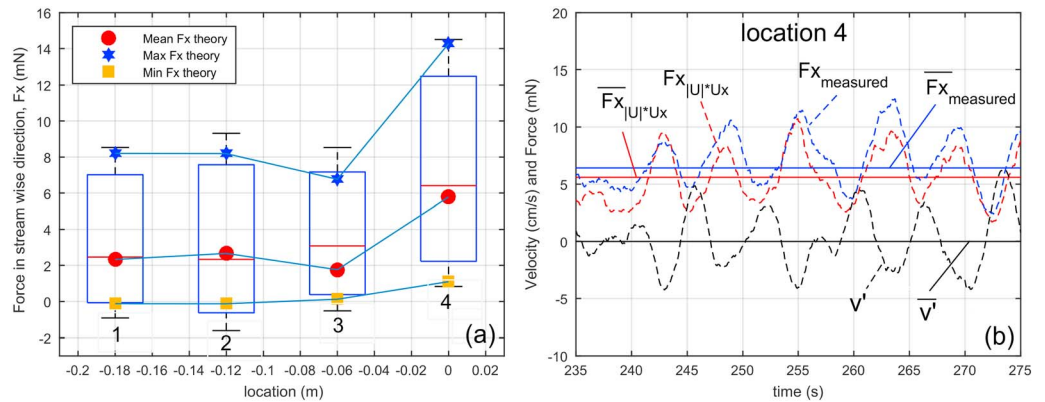


**Figure A2.** Representative distribution of measured stem forces on cylinder 1, 2, 3, 4 (location  $y = -0.18, -0.06, -0.12,$  and  $0$  m), together with forces estimated from the theory, that is, the forces estimated from measured streamwise velocity  $U_x$  combined with drag coefficient  $C_d$  equal 1 (a). Directly measured streamwise force,  $F_x$  on the fourth cylinder (floodplain edge), compared with the forces estimated from the theory. Corresponding lateral velocity fluctuation also included (b). Sparse scenario, 25 cm floodplain width, discharge = 80 L/s, water depth = 14 cm.

wires was placed about 15 cm ahead from the ADV. Very small oxygen bubbles produced by the electrolyzer significantly improved the quality of the ADV signal. In the experiments, the correlations are larger than 85–95%, and the dimensionless signal-to-noise ratios exceed 18 dB in all measurement scenarios. In order to eliminate the formation of calcium carbonate, the electrolyzer was cleaned every 2 hr. The final data were collected applying Nortek software for the Vectrino. With the purpose of capturing a velocity profile over the cross-section, in the slope region with changed water depth, at least 10 points were taken at middepth, while in the region with constant water depth, at least 3 points were measured. Mid-depth measurements means that the distance from the measurement point to the bed changes with flow depth across the lateral profile. Assuming a velocity profile that is either uniform or logarithmic over the vertical, the uncertainty of the depth average velocity measurement is of about 5%.

Particle Image Velocimetry was used to measure the movement of flow. In order to achieve sufficient contrast between the particles and the flume bottom, floating black polypropylene tracer particles with a diameter of around 2 mm were used. Besides, the flume bottom at the capture area was also painted with high contrast white paint. In the present experiments, a sampling frequency of 10 Hz was used. A RedLake 1 MegaPixel digital camera with a resolution of  $1,008 \times 1,018$  pixels has been used to capture frames and was installed on the very top of a frame build on a movable platform constructed over the flume. In order to minimize distortion effects, the digital camera was carefully directed vertically downward. For each measurement with a different water level, a careful check of image distortion was employed. In order to capture most of the features of the water surface flow, a large number of tracer particles was used (Muste et al., 2008). They are expected to follow the surface flow sufficiently well. Their distribution over the water surface was relatively homogeneous. A preprocessing step was applied to enhance the quality of the images. All images were subtracted from a representative background image in order to eliminate undesirable effects of the background information. Then all pairs of sequential camera frames were loaded in Particle Image Velocimetry Lab 1.4 software package and subsequently spatially correlated (Thielicke & Stamhuis, 2014). All sets of two consecutive particle-frames have been analyzed. A two-stage square interrogation windows size of 128 pixels and 32 pixels, respectively, have been used with a spatial overlap of 50% in both  $x$  and  $y$  direction. The measurement duration was 300 s. This means that with a 10 Hz frequency, 3,000 frames were recorded for each case. The average particle displacement has been computed to acquire the instantaneous surface velocity fields.

Figure A2a shows the distribution of measured streamwise stem forces  $F_x$  by box plots at these different locations. The mean value is given by the red line with the box indicating the 25th and 75th percentiles. The mean values of the streamwise forces based on the measured velocity  $U$  are also included in the figure (solid red circles).  $F_{x,theory} = \frac{1}{2} \rho C_d d H |U| U_x$  where  $\rho$  is water density,  $C_d$  is drag coefficient and equal 1,  $d$  is the diameter of the cylinder,  $H$  is water depth,  $|U| = \sqrt{U_x^2 + U_y^2}$  and  $U_x, U_y$  are the mean streamwise and lateral velocity inside the vegetation.

Figure A2b shows the time series of the streamwise force ( $F_x$ ) measured on the fourth cylinder together with the predicted one ( $F_{x,theory}$ ) and the lateral fluctuation velocity ( $v'$ ). It is suggested that the force achieves its maximum value together with the minimum lateral fluctuation velocity ( $v' < 0$ ). This indicates that the force on the cylinder is largest during the sweeps and smallest during the ejections. Furthermore, it is also suggested that a good estimation for the force on the cylinder can be achieved with the value of the drag coefficient  $C_d$  equal 1 combined with the local velocity.

It is noted from the table that there is a large difference between the values of the vegetation drag ( $Cda_{measured}$ ) derived from a balance between total array drag and the pressure gradient due to the free surface slope (see White & Nepf, 2008,  $Cda_{measured} \approx -2gS/U_1^2$ ;  $U_1$  is the cross-sectionally averaged velocity within the vegetation array; and  $S = dh/dx$  is the water slope) and that derived based on the theory ( $Cda_{theory} = Cd_{theory} \cdot N \cdot d$ ;  $Cd = 1$  proved by directly measured forces; see Table A1). This difference can be explained in terms of (1) the presence of reverse flows and stagnant flows which may reduced the averaged streamwise velocity inside the vegetation; (2) mean force is not propotional to the mean velocity squared; and (3) the uncertainty in the measurement of the water slope which in our case is about 20%. This difference can be improved using  $Cda_{|U|U_x} = \frac{-2gS}{\sqrt{U_x^2 + U_y^2} \cdot U_x}$ .

## A2. Similar Laboratory Studies

**Table A3**  
Some Previous Experiments With Similar Configuration

| No | Experiment overall   | Author                            | Year             | Feature    |              |     |
|----|--|-----------------------------------|------------------|------------|--------------|-----|
|    |  |                                   |                  | Vegetation | Floodplain   | HCS |
| 1  | Compound channels  | Knight and Demetriou              | 1983             | N          | Y (vertical) | N   |
| 2  | Overbank flow with vegetated floodplain                    | Pasche and Rouve                  | 1985             | Y          | Y (1:1.5)    | N   |
| 3  | Large Eddies in compound channels                          | Tamai et al.                      | 1986             | N          | Y (vertical) | Y   |
| 4  | Flow in main channel and floodplain                        | Keller and Rodi                   | 1988             | N          | Y (vertical) | N   |
| 5  | Turbulent measurements in shear layer-compound channels    | Shiono and Knight                 | 1988, 1989, 1990 | Y          | Y (1:1)      | Y   |
| 6  | Drag, turbulence and diffusion through emergent vegetation | Nepf                              | 1999             | Y          | N            | N   |
| 7  | 2-D solution for straight and meandering flow              | Ervine et al.                     | 2000             | N          | Y (1:1)      | N   |
| 8  | Turbulence structure in vegetated open channels            | Nezu and Onitsuka                 | 2001             | Y          | N            | Y   |
| 9  | Confluence experiment; Compound channels                   | van Prooijen, Uijtewaal and Booij | 2000, 2004, 2005 | N          | Y (1:1)      | Y   |
| 10 | Mangrove affect flow in a flume                            | Struve et al.                     | 2003             | Y          | N            | N   |
| 11 | Large Coherent Structures in compound channels             | Bousmar and Zech                  | 2004             | N          | Y (vertical) | Y   |
| 12 | Riprap vegetation on near bank turbulence                  | McBride et al.                    | 2007             | Y          | Y (1:1)      | N   |
| 13 | Floodplain Vegetated Channels                              | Mazurczyk                         | 2007             | Y          | Y (1:1)      | N   |
| 14 | Vegetated channels   | White and Nepf                    | 2007, 2008       | Y          | N            | Y   |
| 15 | Vegetated channels—Mean drag                               | Tanino and Nepf                   | 2008             | Y          | N            | Y   |
| 16 | Vegetated channels—sediment                                | Zong and Nepf                     | 2010             | Y          | N            | Y   |
| 17 | Emerged vegetation in compound channels                    | Jahra et al.                      | 2011             | Y          | Y (vertical) | N   |
| 18 | Discharge prediction compound channels                     | Lambert and Sellin                | 1996             | N          | Y (vertical) | N   |
| 19 | Turbulent kinetic energy in compound channels              | Kozioł                            | 2011             | Y          | Y (1:1)      | N   |
| 20 | Vegetated channels -flexible plant                         | Siniscalchi et al.                | 2012             | Y          | N            | Y   |
| 21 | Vegetated channels   | Buckman                           | 2013             | Y          | N            | Y   |
| 22 | Vegetated floodplain channels                              | Hamidifar and Omid                | 2013             | Y          | Y (vertical) | Y   |
| 23 | Vegetated floodplain channels                              | Fernandes et al.                  | 2014             | Y          | Y (vertical) | N   |
| 24 | Flow structure in vegetated channels                       | Yan et al.                        | 2016             | Y          | N            | Y   |
| 25 | Mixing layer development in compound channel flows         | Dupuis et al.                     | 2017             | Y          | Y (vertical) | Y   |

## Acknowledgments

This study is supported by the Ministry of Education and training scholarship (MOET), Vietnam, the Delft University of Technology, the Netherlands and The Thuy Loi University Hanoi, Vietnam. The data used are listed in the references, tables, figures, and appendices.

## References

- Bousmar, D., & Zech, Y. (2004). Large-scale coherent structures in compound channels. In *Shallow Flows: Research Presented at the International Symposium on Shallow Flows, Delft, Netherlands, 2003*, Taylor & Francis (pp. 347).
- Buckman, L. (2013). Hydrodynamics of partially vegetated channels: Stem drag forces and application to an in-stream wetland concept for tropical urban drainage systems, TU Delft.
- Chu, V. H., & Babarutsi, S. (1988). Confinement and bed-friction effects in shallow turbulent mixing layers. *Journal of hydraulic engineering*, *114*(10), 1257–1274.
- Dupuis, V., Proust, S., Berni, C., & Paquier, A. (2017). Mixing layer development in compound channel flows with submerged and emergent rigid vegetation over the floodplains. *Experiments in Fluids*, *58*(4), 30.
- Ervine, D. A., Babaeyan-Koopaei, K., & Sellin, R. H. J. (2000). Two-dimensional solution for straight and meandering overbank flows. *Journal of Hydraulic Engineering*, *126*(9), 653–669.
- Fernandes, J. N., Leal, J. B., & Cardoso, A. H. (2014). Improvement of the lateral distribution method based on the mixing layer theory. *Advances in Water Resources*, *69*, 159–167.
- Hamidifar, H., & Omid, M. H. (2013). Floodplain vegetation contribution to velocity distribution in compound channels. *Journal of Civil Engineering and Urbanism*, *3*(6), 357–361.
- Horstman, E. (2014). The mangrove tangle. Short-term bio-physical interactions in coastal mangroves, (PhD thesis).
- Ikeda, S., Kawamura, K., Fukumoto, M., & Sano, T. (2000). Organized horizontal vortices and lateral sediment transport in compound open channel flows with bank vegetation. *Proceedings of Hydraulic Engineering*, *44*, 795–800.
- Jahra, F., Kawahara, Y., Hasegawa, F., & Yamamoto, H. (2011). Flow-vegetation interaction in a compound open channel with emergent vegetation. *International Journal of River Basin Management*, *9*(3-4), 247–256.
- Jirka, G. H., & Uijtewaal, W. (2004). Shallow flows: A definition. In *Proceedings of the international conference on shallow flows* (pp. 3–11). Delft, Netherlands: Balkema.
- Keller, R. J., & Rodi, W. (1988). Prediction of flow characteristics in main channel/flood plain flows. *Journal of Hydraulic research*, *26*(4), 425–441.
- Knight, D. W., Aya, S., Ikeda, S., Nezu, I., & Shiono, K. (2007). Flow and sediment transport in compound channels, the experiences of Japanese and UK Research. In I. Syunsuke, & Ian K. McEwan (Eds.), *Chap. 2: Flow structure, IAHR Monographs* (pp. 5–113). CRC Press.
- Knight, D. W., & Demetriou, J. D. (1983). Flood plain and main channel flow interaction. *Journal of Hydraulic Engineering*, *109*(8), 1073–1092.
- Knight, D. W., & Shiono, K. (1990). Turbulence measurements in a shear layer region of a compound channel. *Journal of Hydraulic Research*, *28*(2), 175–196.
- Knight, D. W., & Shiono, K. (1996). River channel and floodplain hydraulics. Floodplain processes (pp. 139–181).
- Kozioł, A. (2011). Turbulent kinetic energy of water in a compound channel. *Annals of Warsaw University of Life Sciences-SGGW Land Reclamation*, *43*(2), 193–205.
- Lambert, M. F., & Sellin, R. H. J. (1996). Discharge prediction in straight compound channels using the mixing length concept. *Journal of Hydraulic Research*, *34*(3), 381–394.
- Mazda, Y., Wolanski, E., King, B., Sase, A., Ohtsuka, D., & Magi, M. (1997). Drag force due to vegetation in mangrove swamps. *Mangroves and Salt Marshes*, *1*(3), 193–199. <https://doi.org/10.1023/A:1009949411068>
- Mazurczyk, A. (2007). Scales of turbulence in compound channels with trees on floodplains. *Publications of the Institute of Geophysics, Polish Academy of Science*, *401*, 169–176.
- McBride, M., Hession, W. C., Rizzo, D. M., & Thompson, D. M. (2007). The influence of riparian vegetation on near-bank turbulence: A flume experiment. *Earth Surface Processes and Landforms*, *32*(13), 2019–2037.
- Mihailovic, D., Mimic, G., Gualtieri, P., Arsenic, I., & Gualtieri, C. (2017). Randomness representation of turbulence in canopy flows using Kolmogorov complexity measures. *Entropy*, *19*, 519.
- Muste, M., Fujita, I., & Hauet, A. (2008). Large-scale particle image velocimetry for measurements in riverine environments. *Water Resources Research*, *44*, W00D19. <https://doi.org/10.1029/2008WR006950>
- Nadaoka, K., & Yagi, H. (1998). Shallow-water turbulence modeling and horizontal large-eddy computation of river flow. *Journal of Hydraulic Engineering*, *124*(5), 493–500. [https://doi.org/10.1061/\(ASCE\)0733-9429\(1998\)124:5\(493\)](https://doi.org/10.1061/(ASCE)0733-9429(1998)124:5(493))
- Nepf, H. M. (1999). Drag, turbulence, and diffusion in flow through emergent vegetation. *Water Resources Research*, *35*(2), 479–489.
- Nepf, H. M. (2012). Hydrodynamics of vegetated channels. *Journal of Hydraulic Research*, *50*(3), 262–279. <https://doi.org/10.1080/00221686.2012.696559>
- Nezu, I., & Onitsuka, K. (2001). Turbulent structures in partly vegetated open-channel flows with LDA and PIV measurements. *Journal of Hydraulic Research*, *39*(6), 629–642. <https://doi.org/10.1080/00221686.2001.9628292>
- Nezu, I., Onitsuka, K., & Iketani, K. (1999). Coherent horizontal vortices in compound open-channel flows. In V. P. Singh, I. W. Seo, & J. H. Sonu (Eds.), *Hydraulic Modeling* (pp. 17–32). Colorado: Water Resources Publication.
- Nikora, V. (1999). Origin of the “–1” spectral law in wall-bounded turbulence. *Physical Review Letters*, *83*(4), 734.
- Partheniades, E. (1965). Erosion and deposition of cohesive soils. *Journal of the Hydraulics Division*, *91*(1), 105–139.
- Pasche, E., & Rouve, G. (1985). Overbank flow with vegetatively roughened flood plains. *Journal of Hydraulic Engineering*, *111*(9), 1262–1278. [https://doi.org/10.1061/\(ASCE\)0733-9429\(1985\)111:9\(1262\)](https://doi.org/10.1061/(ASCE)0733-9429(1985)111:9(1262))
- Perry, A. E., & Li, J. D. (1990). Experimental support for the attached-eddy hypothesis in zero-pressure-gradient turbulent boundary layers. *Journal of Fluid Mechanics*, *218*, 405–438.
- Phan, L. K., van Thiel de Vries, J. S. M., & Stive, M. J. F. (2015). Coastal mangrove squeeze in the Mekong Delta. *Journal of Coastal Research*, *30*, 233–243. <https://doi.org/10.2112/JCOASTRES-D-14-00049.1>
- Pope, S. B. (2000). *Turbulent flows*. New York: Cambridge University Press/Cornell University. <https://doi.org/10.1017/CBO9780511840531>
- Ranasinghe, R., Narayan, S., Suzuki, T., Stive, M. J. F., Ursem, W. N. J., & Verhagen, H. J. (2010). On the effectiveness of mangroves in attenuating cyclone induced waves. In *Proceedings of the 32th International Conference on Coastal Engineering, ICCE 2010 June/July, Shanghai*. ASCE-Texas Digital Library (pp. 1–12).
- Shiono, K., & Knight, D. W. (1988). Two-dimensional analytical solution for a compound channel. In *Proceedings, 3rd International Symposium on refined flow modeling and turbulence measurements* (pp. 503–510).
- Shiono, K., & Knight, D. W. (1989). Transverse and vertical Reynolds stress measurements in a shear layer region of a compound channel. In *Proceedings 7th Symposium Turb. Shear Flows* (Vol. 28, pp. 1–6).
- Shiono, K., & Knight, D. W. (1990). Mathematical models of flow in two or multi stage straight channels. In *Proceedings International Conference on River Flood Hydraulics* (pp. 229–238). New York: Wiley.

- Siniscalchi, F., Nikora, V. I., & Aberle, J. (2012). Plant patch hydrodynamics in streams: Mean flow, turbulence, and drag forces. *Water Resources Research*, *48*, W01513. <https://doi.org/10.1029/2011WR011050>
- Struve, J., Falconer, R. A., & Wu, Y. (2003). Influence of model mangrove trees on the hydrodynamics in a flume, Estuarine. *Coastal and Shelf Science*, *58*(1), 163–171.
- Tamai, N., Asaeda, T., & Ikeda, H. (1986). Study on generation of periodical large surface eddies in a composite channel flow. *Water Resources Research*, *22*(7), 1129–1138. <https://doi.org/10.1029/WR022i007p01129>
- Tanino, Y., & Nepf, H. M. (2008). Laboratory investigation of mean drag in a random array of rigid, emergent cylinders. *Journal of Hydraulic Engineering*, *134*(1), 34–41.
- Thielicke, W., & Stamhuis, E. J. (2014). PIVlab—Towards User-friendly, Affordable and Accurate Digital Particle Image Velocimetry in MATLAB. *Journal of Open Research Software*, *2*(1), e30. <https://doi.org/10.5334/jors.bl>
- Truong, S. H., Ye, Q., & Stive, M. J. F. (2017). Estuarine mangrove squeeze in the Mekong Delta, Vietnam. *Journal of Coastal Research*, *33*, 747–763. <https://doi.org/10.2112/JCOASTRES-D-16-00087.1>
- Uijttewaal, W. S. J., & Booij, R. (2000). Effects of shallowness on the development of free-surface mixing layers. *Physics of fluids*, *12*(2), 392–402.
- van Prooijen, B. C. (2004). Shallow mixing layers, (PhD thesis).
- van Prooijen, B. C., Battjes, J. A., & Uijttewaal, W. S. J. (2005). Momentum exchange in straight uniform compound channel flow. *Journal of Hydraulic Engineering*, *131*(3), 175–183. [https://doi.org/10.1061/\(ASCE\)0733-9429\(2005\)131:3\(175\)](https://doi.org/10.1061/(ASCE)0733-9429(2005)131:3(175))
- Vargas-Luna, A., Crosato, A., & Uijttewaal, W. S. J. (2015). Effects of vegetation on flow and sediment transport: Comparative analyses and validation of predicting models. *Earth Surface Processes and Landforms*, *40*(2), 157–176.
- Wallace, J. M. (2016). Quadrant analysis in turbulence research: History and evolution. *Annual Review of Fluid Mechanics*, *48*, 131–158.
- White, B. L., & Nepf, H. M. (2007). Shear instability and coherent structures in shallow flow adjacent to a porous layer. *Journal of Fluid Mechanics*, *593*, 1–32. <https://doi.org/10.1017/S0022112007008415>
- White, B. L., & Nepf, H. M. (2008). A vortex-based model of velocity and shear stress in a partially vegetated shallow channel. *Water Resources Research*, *44*, W01412. <https://doi.org/10.1029/2006WR005651>
- Xiaohui, S., & Li, C. W. (2002). Large eddy simulation of free surface turbulent flow in partly vegetated open channels. *International Journal for Numerical Methods in Fluids*, *39*(10), 919–938. <https://doi.org/10.1002/flid.352>
- Yan, X.-F., Wai, W.-H. O., & Li, C.-W. (2016). Characteristics of flow structure of free-surface flow in a partly obstructed open channel with vegetation patch. *Environmental Fluid Mechanics*, *16*(4), 807–832.
- Zong, L., & Nepf, H. M. (2010). Flow and deposition in and around a finite patch of vegetation. *Geomorphology*, *116*(3–4), 363–372. <https://doi.org/10.1016/j.geomorph.2009.11.020>